


REPORT DOCUMENTATION PAGE		Form Approved OMB No. 0704-0188	
Public reporting burden for this collection of information is estimated to average 1 hour per response, including the time for reviewing instructions, searching existing data sources, gathering and maintaining the data needed, and completing and reviewing the collection of information. Send comments regarding this burden estimate only, other aspect of this collection of information, including suggestions for reducing this burden, to Washington Headquarters Services, Directorate for Information Operations and Reports, 1215 Jefferson Davis Highway, Suite 1204, Arlington VA 22202-4302, and to the Office of Management and Budget, Paperwork Reduction Project (07804-0188), Washington, DC 20503.			
1. AGENCY USE ONLY (LEAVE BLANK)	2. REPORT DATE 21 August 1995	3. REPORT TYPE AND DATES COVERED Professional Paper	
4. TITLE AND SUBTITLE  Aeroelastic Analysis of Transient Blade Dynamics During Shipboard Engage/Disengage Operations		5. FUNDING NUMBERS  	
6. AUTHOR(S)  William P. Geyer, Jr. Edward C. Smith			
7. PERFORMING ORGANIZATION NAME(S) AND ADDRESS(ES)  Visual and Technical Information Branch 7.2.4.3.A, Mail Stop 2, Bldg. 405 Naval Air Warfare Center Aircraft Division Patuxent River, Maryland 20670-5304		8. PERFORMING ORGANIZATION REPORT NUMBER	
9. SPONSORING/MONITORING AGENCY NAME(S) AND ADDRESS(ES)  Naval Air Systems Command Department of the Navy 1421 Jefferson Davis Highway Arlington, VA 22243		10. SPONSORING/MONITORING AGENCY REPORT NUMBER	
11. SUPPLEMENTARY NOTES			
12a. DISTRIBUTION/AVAILABILITY STATEMENT  Approved for public release, distribution is unlimited.			12b. DISTRIBUTION CODE
13. ABSTRACT (Maximum 200 words)  SEE ATTACHED PAPER			
14. SUBJECT TERMS Combat System Test Bed;R&D,Mobile Demonstration		15. NUMBER OF PAGES 32	
		16. PRICE CODE	
17. SECURITY CLASSIFICATION OF REPORT UNCLASSIFIED	18. SECURITY CLASSIFICATION OF THIS PAGE UNCLASSIFIED	19. SECURITY CLASSIFICATION OF ABSTRACT N/A	20. LIMITATION OF ABSTRACT N/A

19951107 058

DTIC QUALITY INSPECTED 8

# AEROELASTIC ANALYSIS OF TRANSIENT BLADE DYNAMICS DURING SHIPBOARD ENGAGE/DISENGAGE OPERATIONS

William P. Geyer Jr.  
Flight Test Engineer  
Naval Air Warfare Center-Aircraft Division  
Patuxent River, Maryland

AUG 21 1995  
Edward C. Smith  
Assistant Professor of Aerospace Engineering  
Pennsylvania State University  
University Park, Pennsylvania

## NOTATION

$e_f$	Flap hinge offset	$t$	Time
$e_g$	Chordwise offset of blade center-of-mass ahead of elastic axis	$t_1$	Initial time
$El_{yy}$	Flap bending stiffness	$t_2$	Final time
$e$	Modal space displacement vector	$T$	Kinetic energy of the blade
$g$	Acceleration due to gravity	$u_F$	Radial foreshortening term
$GJ$	Torsional Stiffness	$U$	Total potential energy
$h_{cg}$	Vertical distance to hub with respect to ship coordinate system	$U_B$	Potential (strain) energy of the blade
$\hat{i}_\xi, \hat{j}_\eta, \hat{k}_\zeta$	Unit vectors of deformed coordinate system	$U_{DS}$	Potential energy of the droop stop
$\hat{I}_I, \hat{J}_I, \hat{K}_I$	Unit vectors of inertial coordinate system	$U_{PL}$	Potential energy of the pitch link
$\hat{I}_H, \hat{J}_H, \hat{K}_H$	Unit vectors of hub coordinate system	$u$	Eigenvector
$\hat{I}_U, \hat{J}_U, \hat{K}_U$	Unit vectors of undeformed coordinate system	$U$	Vector of eigenvectors used for transformation into modal space
$k_m$	Blade cross-sectional mass radius of gyration	$U_{DS}$	Vector of eigenvectors for cantilevered blade
$k_{m1}, k_{m2}$	Blade cross-sectional mass radius of gyration in the flap and lag directions	$V_{roll}$	Lateral wind component due to roll motion
$K_\beta$	Rotational spring stiffness of droop stop	$V_{vert}$	Vertical wind component in inertial coordinate system
$K_\theta$	Rotational spring stiffness of control system	$V_{wod}$	Relative wind-over-deck in inertial coordinate system
$K$	Stiffness Matrix	$V$	Velocity vector of blade relative to airflow
$L$	Blade section lift	$V_b$	Motion induced blade velocity vector for blade in undeformed frame
$m$	Blade section mass	$V^{gust}$	Velocity of deterministic gust
$m_0$	Referenced blade section mass	$V_w$	Wind velocity for blade in undeformed reference frame
$M$	Mass matrix	$w$	Blade displacement in z direction
$N$	Number of finite beam elements	$w'_{DS}$	Droop stop angle
$N_{dof}$	Number of constrained degrees of freedom	$W$	Total work done
$N_m$	Number of eigenvectors used to approximate solution	$W_{AF}$	Work done by the aerodynamic forces
$q$	Global vector of nodal displacements	$W_G$	Work done by gravitational forces
$Q$	Load vector	$X_H, Y_H, Z_H$	Hub coordinate system
$R$	Blade radius	$X_U, Y_U, Z_U$	Undeformed coordinate system
		$\alpha_S$	Longitudinal shaft angle (positive for shaft tilted aft)
		$\alpha_w$	Angle wind vector above $X_H-Y_H$ plane

*Emell(1)*

$\delta()$	Variation in $()$
$\Delta w'$	Rotation of flap hinge
$\Delta\phi$	Rotation of pitch bearing due to control system flexibility
$\phi$	Elastic twist
$\phi_{max}$	Maximum variation in ship roll angle
$\phi_S$	Ship roll angle
$\eta_r$	Distance from elastic axis to blade three-quarter chord
$\kappa_{lat}, \kappa_{vert}$	Scaling factors of deterministic gusts
$\lambda_i$	Induced inflow
$\mu_x, \mu_y, \mu_z$	Components of advance ratio in hub coordinate system
$\nu_B$	Rotating flap frequency
$\Pi$	Total energy functional
$\theta_0$	Rigid pitch angle due to control pitch and pretwist
$\theta_1$	Total blade pitch resulting from rigid pitch twist and elastic twist
$\theta_{75}$	Collective pitch at 75% blade radius
$\rho_s$	Mass density
$T$	Ship roll period
$\Omega$	Rotor rotational speed
$\Omega_0$	Reference rotor rotational speed
$\xi, \eta, \zeta$	Deformed coordinate system
$\psi$	Rotor blade azimuthal angle
$\psi_{wod}$	Relative wind-over-deck direction
$\bar{\psi}$	Nondimensional time

#### Subscripts and Superscripts

$()'$	$\partial()/\partial x$
$()''$	$\partial^2()/\partial x^2$
$(\dot{\phantom{a}})$	$\partial()/\partial t$
$(\ddot{\phantom{a}})$	$\partial^2()/\partial t^2$
$[]^T$	Transpose of vector or matrix
$()_a$	Inboard node of element
$()_b$	Outboard node of element
$()_i$	$i$ th finite element
$()_m$	Center node of element
$[]_m$	Vector or matrix in modal space
$()_D$	Value referenced to deformed coordinate system
$()_U$	Value referenced to undeformed coordinate system

#### ABSTRACT

An analysis tool has been developed to predict transient aeroelastic rotor response during shipboard engage/disengage sequences. The blade is modeled as an elastic beam undergoing deflections in flap bending and torsion. The blade equation of motion is formulated using Hamilton's principle and spatially discretized using the finite element method. The discretized blade equations of motion are integrated for a specified rotor speed run-up or run-down profile. Blade element theory is used to calculate quasi-steady or unsteady aerodynamic loads in linear and nonlinear regimes. Three different simple wind gust distributions are modeled. Basic ship roll motion characteristics are also included in the shipboard airwake environment. An H-46 rotor system model is developed and shows excellent correlation with experimental static tip deflection and blade natural frequency data. Parametric studies are conducted to systematically investigate the effects of collective and cyclic control settings, droop stop angle, and ship motion on blade response. These studies indicate that collective and cyclic control inputs have a moderate effect on maximum negative tip deflections. Torsion and unsteady aerodynamics are shown to be very important to the blade response at high wind speeds for spatially varying gusts.

#### INTRODUCTION

Shipboard helicopter flight operations occur in an adverse environment as depicted in Figure 1. Larger ships, such as aircraft carriers and amphibious assault ships, have flat flight decks that span the length of the ship with a small island. Depending on the aircraft's position on the flight deck and relative winds, the aircraft could experience large scale turbulence with vortices rolling across the deck. Severe updrafts can also be experienced on upwind portions of the deck edges. Smaller ships, such as destroyers, oilers, and frigates, are not designed to provide an aerodynamically clean environment for flight operations. The flight deck length is a small fraction of the ship length and the flight deck is located on the aft portions of the ship. Large antennae, the mast, and superstructure located ahead of the flight deck contribute to very turbulent airwake around the flight deck area. Sharp edged, flat faced hangars located immediately forward of the flight deck cause large downdrafts and areas of recirculating flow. Small vortices are also produced by the sharp hangar edges. Val Healey [1] discusses the aerodynamic characteristics of different ships and the simulation of the ship/helicopter interface. While

Dist	Special	or
A-1		

on approach, pilots often experience a small region of the approach path that contains highly turbulent air. Ship motion, depending on the sea states, can also increase pilot workload and affect the flow over the flight deck. Extensive experimental testing is required to determine wind conditions conducive to safe helicopter takeoff (launch) and landing (recovery).

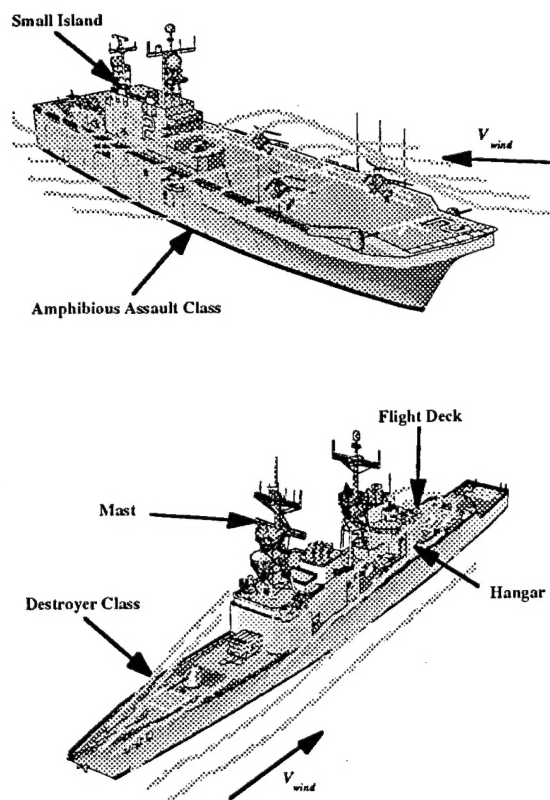


Figure 1: Shipboard aerodynamic environment.

During rotor engage and disengage, the blade passes through low rotor speed regions where aerodynamic forces are large compared to centrifugal stiffening effects. In some conditions, the aeroelastic flapping of the blades becomes large enough for the rotor blades to contact the fuselage. The H-46 Sea Knight, a tandem rotor, medium lift helicopter used by the U.S. Navy and Marines, experiences this blade/fuselage contact during engage/disengage evolutions. It is termed a "tunnel strike" and is depicted in Figure 2. Other aircraft such as the UH-1 Huey, the Westland Lynx, and the H-3 Sea King experience a similar blade-fuselage contact termed a "tailboom strike." Blade-fuselage contact occurs mostly aboard ships in high wind/sea state conditions and has plagued the H-46 Sea Knight since it became operational in 1964. Experimental testing is also required to ensure safe engage/disengage evolutions.

The H-46 has encountered over 100 tunnel strikes since 1964. Most tunnel strikes cause minor damage such as denting or severing the synchronization shaft cover or cracking the synchronization shaft mounts. Major damage involves severing the synchronization shaft, blade failure, or even droop stop failure.

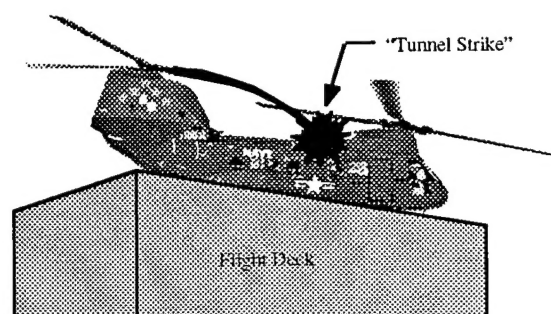


Figure 2: Depiction of tunnel strike.

### Experimental Testing

The Naval Air Warfare Center - Aircraft Division, located in Patuxent River Maryland, conducts all H-46 engage/disengage testing. The goal of this testing is to provide the fleet safe H-46 engage/disengage envelopes. A sample envelope is shown in Figure 3. The shaded area indicates to pilots and ship's personnel the relative wind-over-deck conditions that are conducive to safe engage/disengage evolutions.

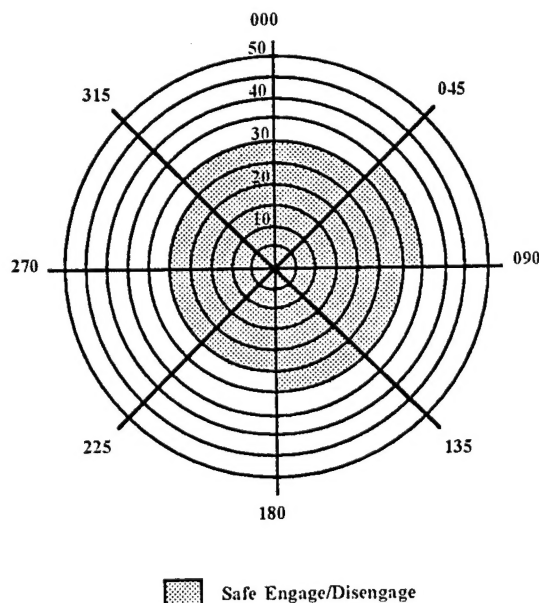


Figure 3: Sample engage/disengage envelope.

Over seven experimental tests were conducted between 1974 and 1987. All provided blade to fuselage clearance data for ship classes certified for H-46 flight operations. Only a few provided qualitative comments on blade behavior and pilot procedures.

Several pilot procedures were incorporated to reduce the chances of a tunnel strike. The speed trim setting (which added longitudinal cyclic pitch to tilt the rotor disk) was changed from "taxi" to "auto" which was found to provide more blade tip-to-fuselage clearance [2]. In addition, pilots were cautioned not to engage if pre-engagement blade flapping was more than a foot at the tips [3, 4].

Engineers made several qualitative comments that aided in defining the tunnel strike phenomenon. Hurley et al. [5] and Ruffa and Traasdaal [6] reported that excessive flapping of the aft rotor blades occurred during the first few rotor revolutions for engagement and the last few rotor revolutions for disengagement. This excessive flapping was believed to be due solely to the horizontal and vertical wind components [5]. While another explanation states that ship motion and turbulence also contributed to this excessive flapping phenomenon [6]. An observation also noted blade behavior under specific testing conditions. The aircraft position relative to the deck edge was believed to have an effect on the blade behavior. The portion of the rotor arc that extended over the flight deck edge was observed to be affected by the airflow more than if the entire rotor disk was over the flight deck [5,6].

#### Analytical Models

Hurst and Newman [7] pioneered the analytical investigation of tail boom strikes in 1985. The hingeless rotor system of the Westland Lynx was modeled using a flapwise elastic rotor code. The first four normal flap modes were used to approximate the blade response. The run-up and run-down rotor speed time histories were predicted using basic rotor system dynamic and blade aerodynamic laws. Gravity terms were included because blade weight and centrifugal stiffening were of the same order of magnitude at low rotor speeds.

The ship airwake environment was modeled by a simple deterministic gust and ship roll motion effects on wind. The deterministic gust was developed from model scale wind tunnel surveys which were correlated with full-scale ship airwake data. Ship motion was modeled as having two effects on the wind encountered by the rotor disk. First, the roll motion caused the rotor disk to encounter both

vertical and lateral wind components and was modeled by varying the wind sinusoidally about the rotor disk. Second, the angular roll rate caused a lateral component of wind at the rotor disk and was added to the existing lateral wind component. Blade element airloads were predicted using static airfoil characteristics including static stall.

Using this analysis, it was predicted that blade fatigue endurance limits could be exceeded with a strong gust (50 knots) and a moderate ship roll motion (7.5 degrees amplitude, 10 second period). Tail boom contact could be induced by a 60 knot wind and a ship roll of 15 degrees with a 10 second period.

Newman [8] continued the tail boom strike work. The fidelity of the model was improved by including a flap-torsion coupling in the aerodynamics. This coupling was independent of rotor speed and representative of the Lynx rotor blade. Detailed wind tunnel experiments were conducted to provide airwake data for the rotor code using the same ship model in the previous paper. This data was also used to modify the existing deterministic gust model.

The existing deterministic gust was characterized by a constant upward wind velocity on the windward half of the rotor disk discontinuous with the constant downward wind velocity on the leeward half of the rotor disk. This gust will be termed a "step gust." The linear gust wind directions (the modified gust model) were the same as the step gust but the spatial variation was linear and continuous over the two halves of the rotor disk. Comparing rotor responses using the two wind gust models and the wind tunnel data, the blade response using the linear gust model was closer to the response using the wind tunnel data. Maximum tip deflections were computed for a strong gust with a linear distribution. It was concluded that flap-torsion coupling and moderate ship motion had a significant effect on the maximum tip deflections.

In 1992, Newman [9] modified the elastic flap code to model articulated (hinged) rotor systems. In this type of rotor, blade motion is constrained to both upper and lower limits using mechanical flap and droop stops. These stops were modeled by using conditional point springs that apply a restraining force a small distance from the flap hinge. Each stop independently retracts and extends at a specific rotor speed for engage and disengage evolutions. The rotor speed run-up and run-down time histories were adjusted for the Sea King's rotor system as well as the gust model to account for the difference in rotor heights above the deck.



The base wind condition used for this study was a strong wind normal to the aircraft's centerline with a linear gust distribution. The vertical components were 20% of the freestream velocity. Tip deflections for the articulated rotor were shown to be much larger than those for the semi-rigid rotor and the inclusion of flap stops further increased the tip deflections.

Newman [10] continued to validate the theoretical model using a wind tunnel model. A helicopter wind tunnel model was constructed from a radio control model which was instrumented to measure flap angle, pitch angle, rotational speed, and blade position. Flap angle and pitch angle were measured using potentiometers. Blade position and azimuth were measured using a transducer. The helicopter model was mounted on a scaled flight deck and subjected to beam winds approaching from the starboard direction. It was found that the largest flap deflections occurred for the hub located a quarter of the deck's width from the windward edge. The mildest flap deflections occurred for the hub located one quarter of the deck's width from the leeward edge; therefore, the influence of the ship's structure is very important to the blade behavior.

#### Present Research

The objective of this research is to develop an analysis capable of predicting transient blade response during shipboard engage/disengage operations. The blade is modeled as an elastic beam undergoing flap and torsion deflections. The finite element method is used for the structural model. This allows nonuniform, articulated or hingeless rotor blades to be modeled very easily and accurately. The discretized blade equations of motion are integrated for a specified rotor speed run-up or run-down profile. Blade element theory is used to calculate quasi-steady or unsteady aerodynamic loads. This analysis supports both linear and nonlinear static airfoil characteristics. A semi-empirical unsteady aerodynamic model based on indicial response is employed to calculate airloads in the attached flow, nonlinear separation and dynamic stall regimes. The present research develops an H-46 blade model and validates it against experimental data. Parametric studies are conducted to systematically investigate the effects of collective and cyclic control settings, droop stop angle, and ship motion on blade response. Furthermore, the importance of torsion and unsteady aerodynamics to the simulation of the transient blade response is determined.

#### THE HELICOPTER MODEL

This analysis predicts the transient aeroelastic response for a single blade of a helicopter with an articulated or hingeless rotor system. The helicopter is resting on the flight deck of a ship with the aircraft's longitudinal axis aligned with the ship's longitudinal axis. A ship can experience six motions, surge, sway, heave, pitch, roll, and yaw, which are illustrated in Figure 4. Ship motion simulation is discussed in Ref. 11 and typical amplitudes and frequencies of the six ship motions are provided. In higher sea states, pitch and roll motions are indicated in Ref. 11 to be more dominant. The present research models ship roll motion to remain consistent with Refs. 7-9. The ship motion frequencies relative to the rotor frequency are small; therefore contributions of ship motion to the blade inertia forces are neglected in the structural model [8]. Only ship roll motion effects on aerodynamics are modeled.

Blade flap (i.e. transverse out-of-plane bending) and torsional deflections are referenced to a plane perpendicular to the shaft axis. The flap and torsion motions are predicted using Bernoulli-Euler beam bending theory. Based upon the assumptions of this theory, the blade is a long slender beam that undergoes small strains but can have moderate deflections. Radial variations in elastic and inertial properties are accommodated by employing the finite element method. Center of gravity and quarter chord offsets from the elastic axis are also varied radially using the finite element method. The analysis can model pretwist and pitch link flexibility.

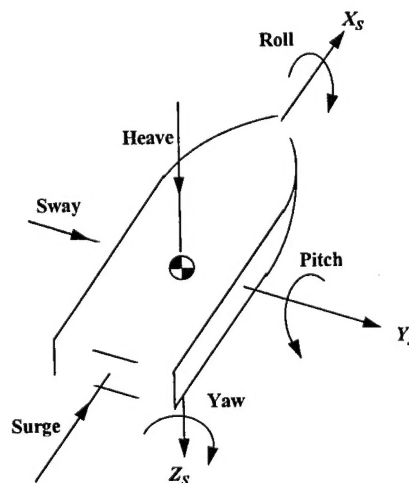


Figure 4: Primary translational and rotational ship motions.

Most of today's rotorcraft codes are designed to predict aircraft trim and stability in hover, forward flight, or steady maneuvers. In these cases, the rotor RPM is  $100 \pm 10$  percent. Blade flap deflections due to gravity are very small and the force of gravity on the blades is neglected. Gravity is very important in this transient analysis because the blade response is required throughout the rotor run-up and run-down sequences. Due to the low rotor speed regions during these sequences, the droop stop is needed to support articulated rotor blades.

### Formulation Using Hamilton's Principle

The partial differential equations governing blade motion are derived using Hamilton's Principle. This energy method uses calculus of variations to minimize the time integral of the difference between kinetic and potential energies for a conservative system from the initial time,  $t_1$ , to the final time,  $t_2$ . The equations of motion for the conservative system are the differential equations contained in the integrand that make the integrand vanish. The aeroelastic system is a nonconservative system and the generalized Hamilton's principle, expressed in Eqn. (1), must be used to derive the blade equations of motion.

$$\delta \Pi = \int_{t_1}^{t_2} (\delta T - \delta U + \delta W) dt = 0 \quad (1)$$

where  $\delta T$  is the variation of kinetic energy,  $\delta U$  is the variation of strain energy, and  $\delta W$  is the virtual work due to external forces.

The variation of strain energy and virtual work are composed of different components due to aerodynamic forces, gravity forces, pitch link stiffness, and droop stop stiffness. The variation of strain energy and virtual work can be expressed as a summation of different contributions and are expressed below

$$\delta U = \delta U_B + \delta U_{DS} + \delta U_{PL} \quad (2)$$

$$\delta W = \delta W_G + \delta W_{AF} \quad (3)$$

where  $\delta U_B$  is the variation of blade strain energy,  $\delta U_{DS}$  is the variation of droop stop strain energy,  $\delta U_{PL}$  is the variation of pitch link strain energy,  $\delta W_G$  is the virtual work due to gravity forces, and  $\delta W_{AF}$  is the virtual work due to the aerodynamic forces.

### BLADE STRAIN ENERGY

Blade strain energy is the potential energy stored in the blade due to deformations. The blade in this analysis is assumed to be a long slender beam with isotropic material properties. This assumption allows the use of only uniaxial stresses ( $\sigma_{yy} = \sigma_{yz} = \sigma_{zz} = 0$ ).

The relationship between uniaxial stresses and classical engineering strains is expressed as

$$\sigma_{xx} = E \epsilon_{xx} \quad (4)$$

$$\sigma_{x\eta} = G \epsilon_{x\eta} \quad (5)$$

$$\sigma_{x\zeta} = G \epsilon_{x\zeta} \quad (6)$$

where  $\epsilon_{xx}$  is the axial strain and  $\epsilon_{x\eta}$  and  $\epsilon_{x\zeta}$  are engineering shear strains.

The blade strain energy equation is

$$U = \frac{1}{2} \int_0^R \iint_A (\sigma_{xx} \epsilon_{xx} + \sigma_{x\eta} \epsilon_{x\eta} + \sigma_{x\zeta} \epsilon_{x\zeta}) d\eta d\zeta dx \quad (7)$$

Performing variational calculus and substituting the axial and engineering shear stresses in Eqn. (7), the nondimensional variation of blade strain energy becomes

$$\delta U = \int_0^1 (U_{w''} \delta w'' + U_{\phi'} \delta \phi') dx \quad (8)$$

where

$$U_{w''} = EI_{yy} \cos^2 \theta_0 w'' \quad (9)$$

$$U_{\phi'} = GJ \phi' \quad (10)$$

$EI_{yy}$  is the flapwise bending stiffness about the  $\eta$  axis and  $GJ$  is the torsional stiffness. A detailed derivation of the variation of blade strain energy can be found in Ref. 12. The reference parameters are dropped for convenience.

### BLADE KINETIC ENERGY

The blade kinetic energy is the energy of the blade due to its velocity. The equation that describes the blades kinetic energy is

$$T = \frac{1}{2} \int_0^R \iint_A \rho_s \mathbf{V}_b \cdot \mathbf{V}_b d\eta d\zeta dx \quad (11)$$

where  $\rho_s$  is the mass density and  $\mathbf{V}_b$  is the blade velocity relative to the hub. The present analysis only requires the flap and twist motion of the blade. Precone and warping are neglected. A radial foreshortening term,  $u_F$ , is used to account for the centrifugal stiffening effects on the flap motion and is defined as

$$u_F = \int_0^x w' \delta w' d\xi \quad (12)$$

A more detailed explanation of this procedure can be found in Ref. 13.

The velocity for the rotating blade relative to the hub is

$$\mathbf{V}_b = V_{b_x} \hat{I}_U + V_{b_y} \hat{J}_U + V_{b_z} \hat{K}_U \quad (13)$$

where

$$\begin{aligned} V_{b_x} = & \dot{u}_F - \dot{w}'(\eta \sin \theta_1 + \zeta \cos \theta_1) \\ & - (\dot{w}' \dot{\theta}_1 + \Omega) (\eta \cos \theta_1 - \zeta \sin \theta_1) \end{aligned} \quad (14)$$

$$V_{b_y} = \Omega[x + u_F - w'(\eta \sin \theta_1 + \zeta \cos \theta_1)] - \dot{\theta}_1(\eta \sin \theta_1 - \zeta \cos \theta_1) \quad (15)$$

$$V_{b_z} = \dot{w} + \dot{\theta}_1(\eta \cos \theta_1 - \zeta \sin \theta_1) \quad (16)$$

Note that Eqn. (13) does not contain ship motion dependent terms. Ship motion effects are only included in the aerodynamics. Substituting the blade velocity, Eqn. (13), into the variation of kinetic energy, and integrating by parts, the nondimensional variation of kinetic energy becomes

$$\delta T = \int_0^1 (T_w \delta w + T_{w'} \delta w' + T_\phi \delta \phi) dx \quad (17)$$

where

$$T_w = -m\ddot{w} - \ddot{\phi} m e_g \cos \theta_0 - \ddot{\theta}_0 m e_g \cos \theta_0 \quad (18)$$

$$T_{w'} = -x m e_g \Omega^2 \sin \theta_0 - \phi x m e_g \Omega^2 \cos \theta_0 - w' \int_x^1 m \Omega^2 x d\xi \quad (19)$$

$$T_\phi = -\ddot{w} m e_g \cos \theta_0 - \ddot{\phi} m k_m^2 - \ddot{\theta}_0 m k_m^2 - w' x m e_g \cos \theta_0 - m \Omega^2 (k_{m2}^2 - k_{m1}^2) \cos \theta_0 \sin \theta_0 - \phi m \Omega^2 (k_{m2}^2 - k_{m1}^2) \cos 2\theta_0 \quad (20)$$

The blade mass per unit length,  $m$ , is nondimensionalized using the reference mass per unit length,  $m_0$ . The flapwise and chordwise mass moment of inertia per unit length are  $m k_{m1}^2$  and  $m k_{m2}^2$ , respectively. The torsional moment of inertia per unit length is  $m k_m^2$ . All moments of inertia are calculated about the elastic axis. The blade center of gravity offset from the elastic axis is  $e_g$ .

### PITCH LINK STIFFNESS STRAIN ENERGY

In most modern helicopters, the control system has some flexibility to decrease control loads. This flexibility may be built into the swash plate, pitch link, or pitch bearing. The control system flexibility is modeled using a rotational spring placed at a specific radial distance from the hub (shown in Figure 5). The strain energy for a discrete rotational spring is given by

$$U_{PL} = \frac{1}{2} K_\theta (\Delta \phi)^2 \quad (21)$$

where  $K_\theta$  is the rotational spring stiffness and  $\Delta \phi$  is the rotation of the pitch bearing. Taking the variation of this strain energy expression, the equation becomes

$$\delta U_{PL} = K_\theta \Delta \phi \delta(\Delta \phi) \quad (22)$$

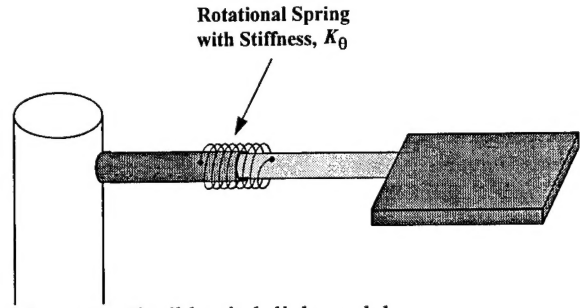


Figure 5: Flexible pitch link model.

### DROOP STOP STIFFNESS

Reviewing the main features of an articulated rotor hub is essential to understanding the flap dynamics for rotor engage/disengage evolutions. A simple hub schematic is shown in Figure 6. Like all articulated rotor hubs, this one contains flap and lag hinges and a method for fastening the blade to the hub, the two-pin retention. The feature most important to the engage/disengage process is the droop stop. During low rotor speeds and at rest, this mechanism restrains the flap hinge from rotating below a certain angle, termed the droop stop angle. At a particular rotor speed, the droop stop will retract during rotor engagement and extend during rotor disengagement. This status also depends on the flap hinge angle.

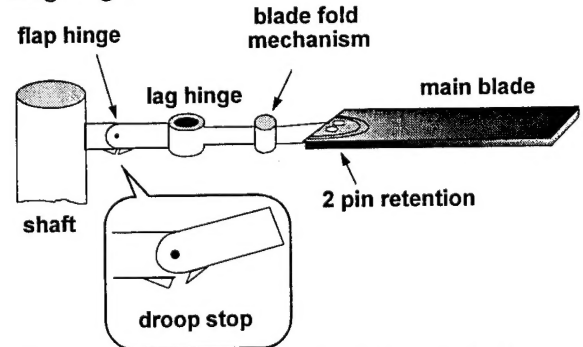


Figure 6: Schematic of an articulated rotor hub.

The droop stop is modeled by a rotational spring as shown in Figure 7. The strain energy for a discrete rotational spring is expressed as

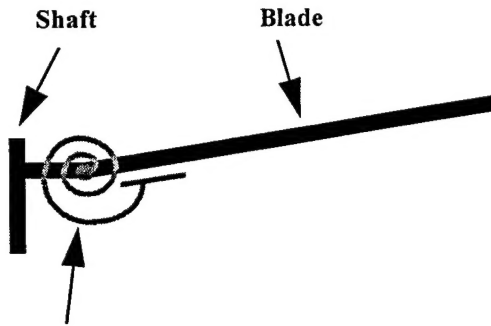
$$U_{DS} = \frac{1}{2} K_\beta (\Delta w' - w'_{DS})^2 \quad (23)$$

where  $K_\beta$  is the rotational spring stiffness,  $\Delta w'$  is the blade rotation at the flap hinge, and  $w'_{DS}$ , droop stop angle, is the specified hinge angle for droop stop



contact. Taking the variation of this strain energy expression, the equation becomes

$$\delta U_{DS} = K_{\beta}(\Delta w' - w'_{DS})\delta \Delta w' \quad (24)$$



**Stiff Conditional Spring in Flap Hinge**

Figure 7: Droop stop model.

The droop stop is a passive mechanism. Centrifugal force acting on a counterweight extends and retracts the droop stop; therefore, the rotational spring stiffness is conditional depending on the rotor speed and hinge angle. Below a specified rotor speed, the droop stop extends. While the droop stop is extended, the rotational spring stiffness is zero for hinge angles greater than the droop stop angle and very large for hinge angles below the droop stop angle. Two other cases must be modeled to ensure proper physical behavior of the droop stop. During rotor engagement, the blade may be in contact with the droop stop upon reaching the rotor speed at which the droop stop can retract. The droop stop cannot retract until the blade lifts off of the droop stop. During rotor disengagement, the hinge angle may be below the droop stop angle upon reaching the rotor speed at which the droop stop can extend. The hinge angle must be above the droop stop angle to enable the droop stop to extend. The program uses simple logic to model the physical behavior of the droop stop.

### GRAVITATIONAL FORCES

As stated earlier, gravitational forces are required in this analysis due to their effect on blade deflection over the low rotor speed regions. The work performed on the blade due to gravitational forces is expressed as

$$W_G = - \int_0^R mg \hat{K}_I \cdot w \hat{K}_U dx \quad (25)$$

where  $g$  is the acceleration due to gravity (assumed downward acceleration positive). This analysis assumes that the ship motion effects on inertia and

the shaft tilt angles are small; therefore, the nondimensional virtual work is expressed as

$$\delta W_G = - \int_0^1 mg \delta w dx \quad (26)$$

### Blade Equations of Motion

The generalized Hamilton's principle, Eqn. (1), is being used to formulate the blade equations of motion. The finite element method is used to formulate the discretized blade equations of motion. The nondimensional virtual energy expression for the discretized blade can be written as

$$\delta \Pi = \int_{\bar{\psi}_1}^{\bar{\psi}_2} \left[ \sum_{i=1}^N (\delta T_i - \delta U_i + \delta W_i) \right] d\bar{\psi} \quad (27)$$

where  $i$  is the  $i$ th beam element and  $N$  is the total number of beam elements in blade.

An illustration of the blade finite element discretization is shown in Figure 8. Each of the  $N$  flexible elements has three nodes, two external and one internal, which describe the elemental displacements. Each external node has  $w$ ,  $w'$ , and  $\phi$  nodal displacements and the internal node only has a  $\phi$  nodal displacement. This gives seven degrees of freedom ( $w_a$ ,  $w'_a$ ,  $\phi_a$ ,  $\phi_m$ ,  $w_b$ ,  $w'_b$ , and  $\phi_b$ ) for the  $i$ th element. Deformations in the element are described by shape functions.

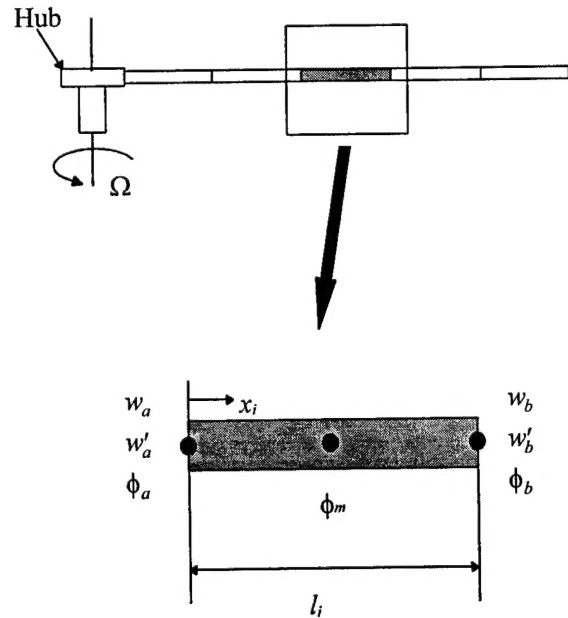


Figure 8: Blade elemental degrees of freedom.

The shape functions discretize the virtual energy expression for each element. The shape functions are interpolation functions derived from a cubic Hermitian polynomial for flap deformation and a

quadratic Lagrangian polynomial for torsion deformation. A detailed description of the shape functions is given in Ref.12.

The energy expressions are spatially discretized by substituting the shape functions into the elemental virtual energy expressions. The resulting expressions are integrated in space using a six point Gaussian Quadrature method. The virtual energy expression in terms of the elemental matrices and load vector becomes

$$\delta\Pi = \int_{\bar{\psi}_1}^{\bar{\psi}_2} \left[ \sum_{i=1}^N \delta\mathbf{q}_i^T (\mathbf{M}_i \ddot{\mathbf{q}}_i + \mathbf{C}_i \dot{\mathbf{q}}_i + \mathbf{K}_i \mathbf{q}_i - \mathbf{Q}_i) \right] d\bar{\psi} \quad (28)$$

where  $\mathbf{M}_i$ ,  $\mathbf{C}_i$ , and  $\mathbf{K}_i$ , are the elemental mass, damping and stiffness matrices, respectively, and  $\mathbf{Q}_i$  is the elemental load vector.

These elemental mass, damping and stiffness matrices and load vector are assembled to form their global counterparts. The assembly process provides flexibility in modeling different types of rotor systems which makes the finite element method very powerful. A cantilever condition between the  $i$  and  $i-1$  elements is achieved by letting the elemental degrees of freedom have the same global degrees of freedom at the common node. The assembly procedure can be easily modified to accommodate a flap hinge, pitch bearing, or both. A flap hinge or pitch bearing is accounted for in the assembly by adding an extra global degree of freedom to the node between elements  $i-1$  and  $i$ . In the flap hinge case, the  $(w'_b)_{i-1}$  and  $(w'_a)_i$  elemental degrees of freedom have separate global degrees of freedom. This allows rotation between the elements. The same procedure is followed to model a pitch bearing between two elements using the torsion degree of freedom.

The variations in strain energy for droop stop stiffness and pitch link stiffness are in terms of discrete degrees of freedom that have not been defined to this point. The flap hinge rotation,  $\Delta w'$ , can be expressed as the difference between the elemental degrees of freedom,  $(\Delta w'_a)_i$  and  $(\Delta w'_b)_{i-1}$ . The variation of strain energy due to droop stop stiffness, Eqn (24), becomes

$$\delta U_{DS} = \delta(w'_a)_i K_\beta [(w'_a)_i - (w'_b)_{i-1} - w'_{DS}] - \delta(w'_b)_{i-1} K_\beta [(w'_a)_i - (w'_b)_{i-1} - w'_{DS}] \quad (29)$$

The motion dependent terms would only be added to the *stiffness matrix* and the motion independent terms would only be added to the *load vector*. The treatment for the variation of strain energy for pitch link stiffness is similar and described in Ref. 12.

Once the global mass, damping and stiffness matrices and load vector are assembled, the global

virtual displacements,  $\delta\mathbf{q}$ , are arbitrary and the discretized equations of motion become

$$\mathbf{M}\ddot{\mathbf{q}} + \mathbf{C}\dot{\mathbf{q}} + \mathbf{K}\mathbf{q} = \mathbf{Q} \quad (30)$$

Lastly, kinematic boundary conditions are applied to the global matrices and load vector by setting the degree of freedom that corresponds to boundary condition equal to zero.

### Aerodynamic Modeling

This section discusses the shipboard aerodynamic environment, blade element airload prediction, and calculation of virtual work due to airloads.

### THE AERODYNAMIC ENVIRONMENT

The shipboard aerodynamic environment is characterized by a very complex flowfield. As stated earlier, the ship's superstructure causes highly turbulent flow and ship motion can increase inflow through the rotor disk. In the present study, blade transient response to several simplified deterministic gust distributions are investigated. The ship airwake has been simplified to increase computational efficiency but more importantly to distinguish the effects of certain airwake characteristics on the blade response. The ship is assumed to be stationary with respect to the inertial coordinate system except for roll motion. The atmospheric winds relative to the ship are uniform. These winds are termed the

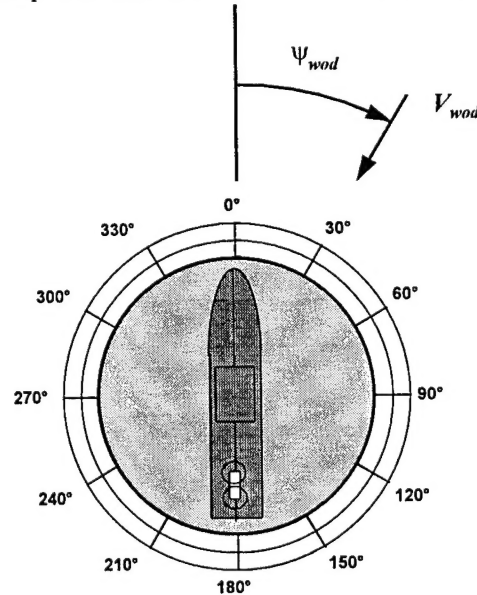


Figure 9: Wind-over-deck convention.

relative Wind-Over-Deck (WOD) conditions. They are defined by a wind speed,  $V_{wod}$ , and direction,  $\psi_{wod}$ , and a vertical wind component,  $V_{vert}$ . The

relative WOD speed and direction describes the wind speed and the direction from which the wind approaches the ship. Figure 9 illustrates the wind direction convention. The vertical wind component follows the sign convention defined by the inertial coordinate system.

### Ship Roll Motion

Recall that roll and pitch were indicated by Ref. 11 to be the dominant ship motions. Roll motion is used in this analysis to remain consistent with Refs. 7-9. The ship roll motion aerodynamic model consists of the transformed relative WOD conditions due to the ship roll angle and a wind component at the hub height due to the angular roll velocity (shown in Figure 10). Ship roll motion is governed by sinusoidal variation of the roll angle,  $\phi_S$ , and can be expressed as

$$\phi_S = \phi_{max} \sin\left(\frac{2\pi\psi}{T}\right) \quad (31)$$

where  $\phi_{max}$  is the maximum roll angle and  $T$  is the nondimensional ship roll period. The roll angular velocity causes a wind velocity along the  $Y_S$  axis at the hub height. This wind component,  $V_{roll}$ , is given by

$$V_{roll} = \phi_{max} h_{cg} \left(\frac{2\pi}{T}\right) \cos\left(\frac{2\pi\psi}{T}\right) \quad (32)$$

where  $h_{cg}$  is the distance along the  $Z_S$  axis from the ship's center of gravity to the aircraft hub.

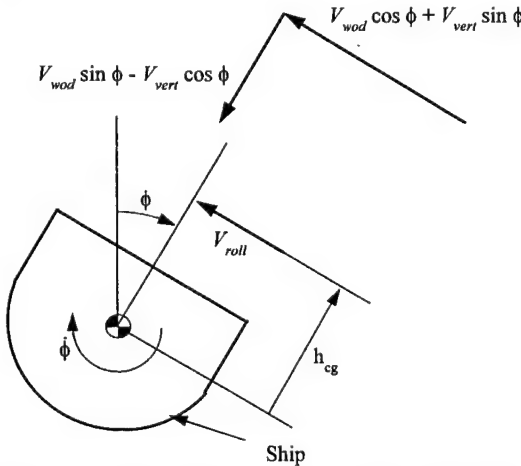


Figure 10: Ship motion effects on wind velocities.

### Deterministic Gust Model

Ship airwake is very unsteady and turbulent. Vortices shed off the ship's superstructure and flow over the flight deck at very random intervals; therefore, the airwake characteristics are very

spatially dependent. Two gust models that simulated the air flow over a ship flight deck subjected to a crosswind were developed in Ref. 8. The step and linear gust models are shown in Figure 11. These models are adopted in this analysis to explore the effects of local wind variations over the disk on the blade response. The deterministic gusts consist of an upward wind component on the windward half of the rotor disk, a downward wind component on the leeward half of the disk, and a lateral wind component in the direction of the relative WOD velocity. The magnitude of these components are specified as fractions of the relative WOD velocity. The wind velocity due to the deterministic gust model can be expressed as

$$\mathbf{V}^{gust} = V_x^{gust} \hat{i}_H + V_y^{gust} \hat{j}_H + V_z^{gust} \hat{k}_H \quad (33)$$

where  $V_z^{gust}$  is the vertical gust component and is dependent on gust model. The other two components are independent of the gust model and defined by

$$V_x^{gust} = V_{wod} \kappa_{lat} \cos(\psi_{wod}) \quad (34)$$

$$V_y^{gust} = -V_{wod} \kappa_{lat} \sin(\psi_{wod}) \quad (35)$$

where  $\kappa_{lat}$  is the fraction of the WOD velocity for the lateral wind components.

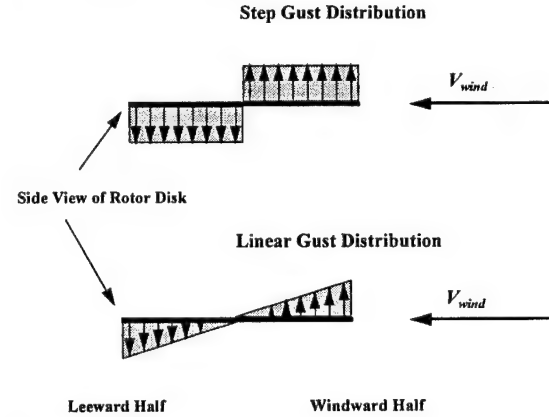


Figure 11: Deterministic wind gusts.

The step gust distribution is characterized by a discontinuity between the windward and leeward halves. The vertical wind velocities are constant over each half of the disk and are defined by

$$V_z^{gust} = V_{wod} \kappa_{vert} \quad (36)$$

where  $\kappa_{vert}$  is the fraction of the WOD velocity and depends on blade position. The direction of the vertical component is negative when the blade is in the leeward half of the disk. The linear gust distribution smoothly transitions from the windward to the leeward half the disk. The vertical gust component is defined as

$$V_z^{gust} = V_{wod} \kappa_{vert} x \cos(\psi - \pi + \psi_{wod}) \quad (37)$$

where unlike the step gust model, this one is a function of blade position and inherently accounts for the direction of the vertical gust component.

### BLADE ELEMENT AIRLOADS

This analysis is able to predict both quasi-steady and unsteady aerodynamic loads and allows many different levels of aerodynamic fidelity. A brief derivation of the resultant velocity in the deformed reference frame is given before details of each aerodynamic model are discussed.

#### Resultant Velocity

The velocity of the blade in the undeformed coordinate system can be expressed as

$$\mathbf{V} = \mathbf{V}_b - \mathbf{V}_w \quad (38)$$

where  $\mathbf{V}_b$  is the motion induced blade velocity and the  $\mathbf{V}_w$  is the wind velocity. The velocity of the rotating blade with respect to the blade undeformed coordinate system was derived earlier (Eqn. 13). Some modifications and substitutions must be made to this equation before using it in this derivation. The axial foreshortening term,  $u_F$ , was used to develop the centrifugal stiffening term in the kinetic energy expression. This term is nonlinear and can be neglected in this derivation. Furthermore thin airfoil theory is only concerned with the resultant velocity at the three-quarter chord ( $\eta = \eta_r$  and  $\zeta = 0$ ). The final form of the motion induced blade velocity components is given by

$$V_{b_x} = -\dot{w}'\eta_r \sin \theta_0 - w'\dot{\theta}_0 \eta_r \cos \theta_0 - \Omega \eta_r (\cos \theta_0 - \phi \sin \theta_0) \quad (39)$$

$$V_{b_y} = \Omega [x - w'\eta_r \sin \theta_0] - \dot{\phi} \eta_r \sin \theta_0 - \dot{\theta}_0 \eta_r (\sin \theta_0 + \phi \cos \theta_0) \quad (40)$$

$$V_{b_z} = \dot{w} + \dot{\phi} \eta_r \cos \theta_0 + \dot{\theta}_0 \eta_r (\cos \theta_0 - \phi \sin \theta_0) \quad (41)$$

Details of this derivation can be found in Ref. 12.

The wind velocity relative to the hub coordinate system of the aircraft is composed of the different components of the ship airwake as described earlier. The nondimensional wind velocity in the undeformed coordinate system is given by

$$\mathbf{V}_w = (\mu_x \cos \psi + \mu_y \sin \psi) \hat{J}_U + (-\mu_x \sin \psi + \mu_y \cos \psi) \hat{J}_U + (\mu_z - \lambda_i) \hat{K}_U \quad (42)$$

where  $\lambda_i$  is the induced inflow and  $\mu_x$ ,  $\mu_y$ , and  $\mu_z$  are defined by

$$\mu_x = V_{wod} \cos \psi_{wod} \cos \alpha_S - V_{vert} \sin \alpha_S \cos \phi_S + V_{wod} \sin \psi_{wod} \sin \alpha_S \sin \phi_S + V_x^{gust} \quad (43)$$

$$\mu_y = -V_{wod} \sin \psi_{wod} \cos \phi_S - V_{vert} \sin \phi_S + V_y^{gust} + V_{roll} \quad (44)$$

$$\mu_z = V_{wod} \cos \psi_{wod} \sin \alpha_S + V_{vert} \cos \alpha_S \cos \phi_S - V_{wod} \sin \psi_{wod} \cos \alpha_S \sin \phi_S + V_z^{gust} \quad (45)$$

Reference parameters are dropped for convenience. The resultant velocity in the undeformed frame is transformed to the deformed frame to obtain the components  $U_R$ ,  $U_P$ , and  $U_T$ . This derivation is shown with greater detail in Ref. 12.

The rotor does not produce any net thrust during rotor engage and disengage evolutions, however a uniform induced inflow is assumed to validate the analysis in other flight regimes. In addition, a linear inflow model, specifically the Drees inflow model, is included to validate the unsteady aerodynamics. The details of this model are described in Ref. 14.

### Quasi-Steady Blade Element Aerodynamics

The quasi-steady aerodynamics development follows a similar unsteady thin airfoil theory development by Johnson [15]. In the unsteady thin airfoil development, the airfoil is modeled by two thin vortex sheets, one being the airfoil and the other a shed wake. Since this is a quasi-static development, the unsteady deficiency function is neglected. This development also includes the airloads due to virtual mass (noncirculatory) effects. The analysis allows either linear or nonlinear predictions. The nonlinear airloads are predicted using Kirchhoff's nonlinear separation model. Figure 12 graphically illustrates the transformation of the quasi-steady airloads from lift, drag and pitching moment at the aerodynamic center to the normal force and pitching moment at the quarter chord. A detailed formulation of the quasi-steady airloads is given in Ref. 12.

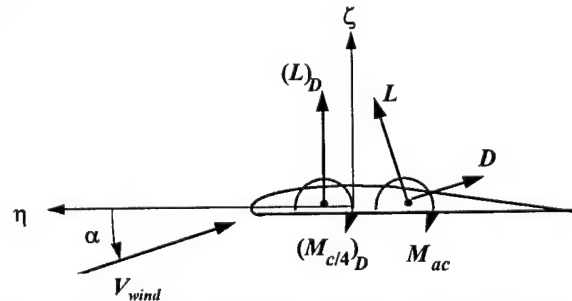


Figure 12: Quasi-steady airloads transformation to deformed frame.

### Unsteady Blade Element Aerodynamics

The unsteady aerodynamic model used in this analysis was developed by Leishman and Beddoes. Significant documentation on the development of this theory can be found in Ref. 14 and Refs. 16-18. The model is divided into three subsystems, attached flow unsteady aerodynamics, nonlinear aerodynamics (trailing edge separation), and dynamic stall. These subsystems are based on the principle of superposition, however they contain some interdependency. The attached flow unsteady aerodynamics subsystem is independent. The nonlinear aerodynamics subsystem depends on the attached flow subsystem for input and the dynamic stall subsystem depends on the nonlinear subsystem for input.

The attached flow unsteady model is based on an indicial response formulation. It predicts both noncirculatory and circulatory airloads. In the case of circulatory airloads, Deficiency functions use exponential functions to model the build-up of the circulatory normal force and pitching moment. Using piston theory, initial values of noncirculatory airloads are determined as functions of Mach number. Exponential functions are used to model the rapid decay of the initial noncirculatory normal force and pitching moment.

A detailed description of the incorporation of Leishman and Beddoes' unsteady aerodynamic model into the present analysis given in Ref. 12.

### Reverse Flow

When helicopters are in forward flight, the rotor blade sees regions of reverse flow on the retreating side of the rotor disk. Similarly, the rotor blade encounters reverse flow for a helicopter resting on the deck in a wind, however, the region in which the blade experiences reverse flow increases with decreasing rotor speed. Figure 13 illustrates the increase in the reverse flow region with decrease in rotor speed. Reverse flow occurs when  $U_T$  is negative. This analysis has included a very simple treatment of reverse flow. The angle of attack is adjusted to maintain the a continuous variation of lift in the deformed coordinate system. Reverse flow effects on the pitching moment are not considered in this analysis. A more advanced treatment of the airfoil behavior in reverse flow can be found in Ref. 15.

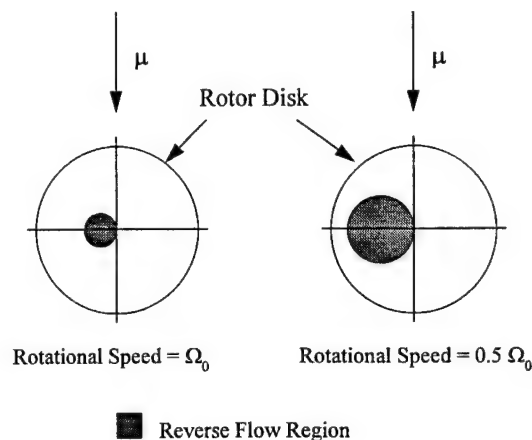


Figure 13: Effects of rotational speed on reverse flow regions.

### FINITE ELEMENT FORMULATION

The airloads are transformed from the deformed frame to the undeformed frame. The virtual work performed by the aerodynamic forces becomes

$$\delta W_{AF} = \int_0^1 [(L)_U \delta w + (M)_U \delta \phi] dx \quad (46)$$

The virtual work term is discretized into  $N$  blade elements and the normal force and pitching moment terms are divided into motion dependent and independent terms. All motion dependent quasi-steady terms are combined with the corresponding elemental mass, stiffness, or damping matrix. All unsteady and motion independent quasi-steady terms are combined with the elemental load vector.

### ANALYSIS

In the previous section, the theory used to model the blade structure and aerodynamic loads was discussed and the method used to discretize the blade equations of motion was described. Three analyses; eigenanalysis, transient response analysis, and engage/disengage envelope analysis, can be performed on the discretized equations of motion. These analyses are interdependent because the eigenanalysis is required for the transient response analysis and the transient response analysis is used in the engage/disengage envelope analysis.

An eigenanalysis is used to determine the blade natural frequencies and mode shapes. This procedure is necessary to ensure that the proper dynamic characteristics of the blade are captured. The natural frequencies must be verified against experimental data from the blade and mode shapes are checked to ensure that the proper boundary conditions are met.

This is the first step before a transient analysis can begin.

The engage/disengage envelope analysis is a tool used to determine the wind conditions for safe engage/disengage sequences as shown in Figure 3. This tool uses the blade transient response to calculate the maximum downward tip deflection for an engage/disengage sequence. The maximum downward tip deflection is rated as safe or unsafe according to blade clearance criteria. This process is performed for many wind-over-deck conditions to form the safe engage/disengage region.

The following subsections provide a detailed discussion of the transient response analysis and the difficulties experienced with the droop stop model.

### Transient Response Analysis

The blade transient response is calculated by integrating the discretized blade equations of motion. The integration is performed by a 4th order Runge-Kutta scheme. The blade static deflection is used as the initial conditions for rotor run-up and is calculated by setting all aerodynamic terms and blade rotational speed to zero. The blade static deflection is also used as the initial conditions for any constant rotor speed solution. For a transient response at a constant rotor speed, the system cannot be perturbed until the blade reaches a steady state response. Similarly, the blade static deflection is used for the initial conditions of a run-down solution. The rotor speed is held constant until a steady state response is reached. After achieving the steady state response, the rotor speed variations follow the specified rotor speed time history.

The blade response can be computed in either physical or modal space. This analysis allows integration in either space but recommends modal space for computational efficiency. Integration in modal space is accomplished by using the  $N_{dof}$  orthogonal eigenvectors as a basis for a linear space; therefore, the response of an  $N_{dof}$  system can be reduced to  $N_{dof}$  independent single degree of freedom systems. This process is called modal analysis. The linear space is called modal space because each independent single degree of freedom system corresponds to a blade structural mode of vibration. The response of each independent mode of vibration combines linearly to determine the physical response of the blade according to the equation

(47)

where  $U$  is the modal vector and  $e$  is the vector of modal coordinates.

The simplification above provides great insight into the contribution of each structural mode to the blade response. Unfortunately, motion dependent aerodynamic loads complicate this simplistic representation. The airloads provide additional mass and stiffness to the corresponding structural matrices and also provide a powerful damping matrix. These combine to form the equations of motion for the aeroelastic system given by

(48)

The damping and stiffness matrices are typically not symmetric and the resulting modal system is no longer an uncoupled set of differential equations. The computational power of the integration in modal space comes from the ability to approximate the blade motion using the first few modes of vibration. The higher modes provide little contribution to the blade response; therefore, only the first  $N_m$  eigenvectors are loaded into the modal vector which can be described by

(49)

This is used in Eqn. (47) to perform the transformation into modal space.

Substituting Eqn. (47) into the blade equation of motion, Eqn. (48), and premultiplying by  $U^T$ , the equations of motion in modal space become

(50)

where  $M_m$ ,  $C_m$ , and  $K_m$  are the modal mass, damping and stiffness matrices, respectively, and  $Q_m$  is the modal load vector.

An important issue when performing a transient analysis is the difference between nondimensional time and blade azimuthal position. These terms are considered the same when integrating the blade equations of motion for a constant rotor speed equal to the reference rotor speed,  $\Omega_0$ . For this analysis, nondimensional time, given in radians, is defined as

(51)

where  $t$  is time in seconds and the reference rotor speed is given in radians per second. The relationship between blade azimuthal position,  $\psi$ , and nondimensional time,  $\bar{t}$ , for rotor run-up is graphically illustrated in Figure 14. At  $t = 0$  seconds,  $\psi$  and  $\bar{t}$  are at an azimuth of zero radians. During every time step,  $\bar{t}$  steps at a constant increment. For times of 1, 2, and 3 seconds, note that  $\psi$  increments are not constant as it approaches the reference rotor speed. At  $t = 4$  seconds,  $\Omega$  reaches the reference rotor speed. For times of 4 and 5 seconds,  $\psi$  takes constant steps equal to  $\bar{t}$  but is not at the same azimuthal position.



### Effects of Droop Stop Behavior on Integration

Recall that a very stiff rotational spring is used to freeze the hinge during blade/droop stop contact. Once the blade lifts off the droop stop the rotational spring is removed from the system. The integration scheme requires smaller time steps to approximate the blade response to discontinuities in rotational spring stiffness. This subsection investigates the effects of the droop stop on integration in modal space.

A simple uniform blade is used to quantify the effects of droop stop contact on the integration. The blade is modeled with 6 elements and the flap hinge is located on the outboard node of the first element. The aerodynamic environment consists of a relative wind approaching from the starboard side of the ship at 50 knots with no vertical wind component. The linear gust distribution and ship roll motion are not used in this study. The blade transient response is found for the run-up rotor speed sequence given in Ref. 9. Integrating in physical space, the 4th order Runge-Kutta method calculates a stable solution using a nondimensional time step of 0.0001 radians.

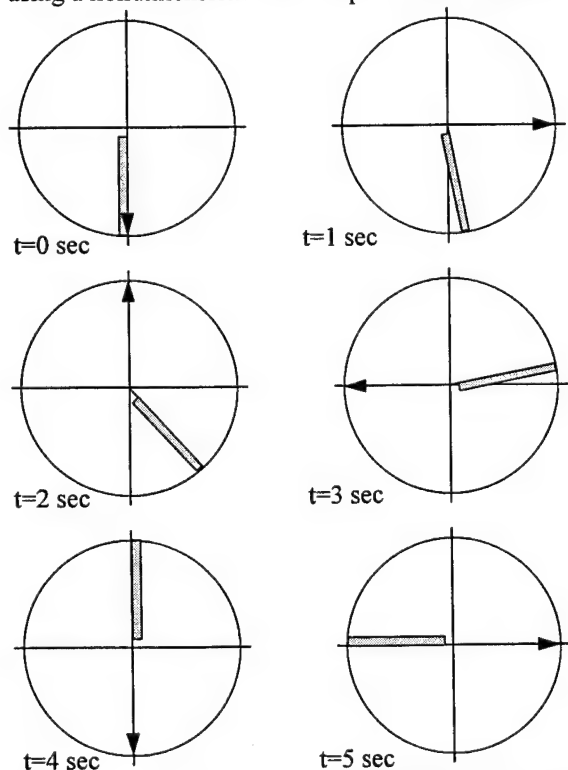


Figure 14: Comparison of nondimensional time and rotor blade azimuth for rotor run-up

Integration in modal space is an effective way to reduce the time required to obtain the transient

response, however droop stop contact affects the accuracy of the response. For the following convergence studies, the blade is divided into eleven elements to ensure accurate flap mode shapes to the tenth mode. The Runge-Kutta integrator is able to compute a converged solution using a time step of 0.0004 radians. Figure 15 compares the solution integrated in physical space to a solution integrated in modal space using nine flap modes, one torsion mode and a nondimensional time step of 0.0004 radians. Accurate transient solutions without blade/droop stop contact can be computed in modal space using only 5 flap modes. Even with 9 flap modes present, note all of the noise in the time histories computed in modal space and the peak negative tip deflection occurs later. Blade deflection during droop stop contact is due purely to elastic deformation with no rigid body rotation at the hinge. The normal modes used to compute this motion do not represent purely elastic deformation and require more flap modes to approximate the blade shape. Even a higher number of normal modes does not accurately predict the blade deformation in the first revolution.

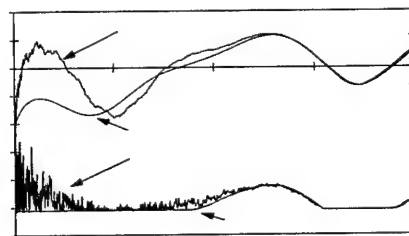


Figure 15: Comparison of blade responses integrated in physical and modal space.

### Modal Swapping Method

The modal swapping technique is developed to circumvent the integration problem in modal space. Before integration begins, an eigensolution is found for the structure with and without the droop stop rotational spring included for  $\Omega/\Omega_0=1$ . The first  $N_m$  eigenvectors for the solution with and without the droop stop rotational spring included are loaded into the modal vectors  $U_{DS}$  and  $U$ , respectively. During integration, the modal vector without the rotational spring effects,  $U$ , is used to transform the system into modal space while there is no blade/droop stop contact; however, when contact occurs, the modal vector with rotational spring effects,  $U_{DS}$ , is used to transform the system into modal space.

Convergence studies are performed to determine the lowest number of modes and the lowest time step necessary for an accurate solution. Only 6 elements

are used to define the blade. Figure 16 illustrates the convergence of the transient blade response computed in modal space using 4 flap modes as a function of time step. A stable transient response could not be found for time steps greater than 0.5 radians. Note that even at a time step of 0.5 radians, the solution is converged. The convergence of the transient response as a function of the number of modes is shown in Figure 17. The solution is barely converged at 4 modes with tip deflections within four percent of the baseline solution.

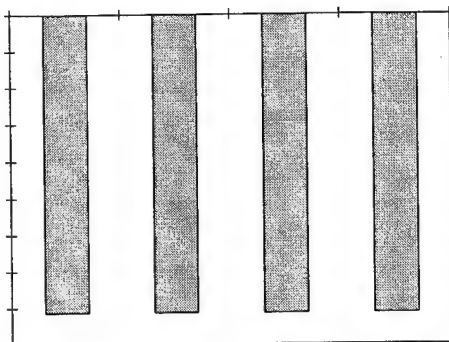


Figure 16: Convergence of blade response as a function of time step.

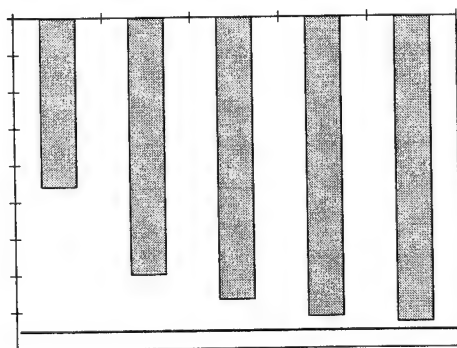


Figure 17: Convergence of blade response as a function of number of modes.

The convergence study performed on the effects of time step give an initial indication of the possible time savings the modal swapping technique can provide. The same number of elements used to obtain the transient solutions in physical space are used for the calculation of the solutions using the modal swapping technique. The modal swapping technique used 6 modes (5 flap and 1 torsion) to

obtain its results. Using a nondimensional time step of 0.0001 radians, the modal swapping technique is approximately 1.6 times faster than the integration in physical space. Optimizing the modal swapping technique to its full potential, the time step is increased to 0.04 radians. The modal swapping technique's speed is 560 times faster than the integration in physical space. This illustrates the savings in time gained by employing the modal swapping technique.

## RESULTS AND DISCUSSION

This analytic capability is kept very general to maintain flexibility. Any articulated or hingeless rotor system can be modeled, however, the results and discussion of this paper focuses on the H-46 Sea Knight. Initially, aircraft specific parameters used to model the H-46 are discussed. Then the blade is validated against experimental data. Finally sensitivity studies are conducted to understand the physics underlying this phenomenon.

### H-46 Model

The H-46 Sea Knight is a medium lift, tandem rotor helicopter with a maximum gross weight of approximately 24000 pounds. Each fully articulated hub has three rotor blades. The fore and aft rotor systems spin in opposite directions where the aft rotor blades spin clockwise when viewed from above. The operational rotor speed of both rotor systems is 27.65 rads/sec (264 RPM). The rotor speed at which the droop stop extends/retracts and the droop stop angle are determined from Navy and Boeing reports. The rotor speed at which the droop stop retracts/extends is approximately 47% of the operational rotor speed [19]. The droop stop angle is not explicitly given as a standard angle in any report and may vary from aircraft to aircraft. Using data from Refs. 19 and 20, the droop stop angle is calculated to be -0.54 degrees.

Each blade is 25.5 feet in length from shaft to tip and has a chord of 1.5625 feet. The Lock number for the H-46 blade is 7.22. All blade structural properties are found in Ref. 21. Variations of  $EI_{yy}$ ,  $GJ$ ,  $m$ ,  $mk_m^2$ , and  $e_g$  with radial station are represented using the finite element approach. The finite element models and the actual variations of  $EI_{yy}$ ,  $GJ$ ,  $m$ ,  $mk_m^2$ , and  $e_g$  with radial station are shown in Ref. 12. Twelve elements are used in the finite element representation of the H-46 blade. The flap hinge is located on the outboard node of the first element and the pitch bearing is located on the outboard node of the second element. The

nondimensional droop stop spring stiffness,  $K_\beta/(m_0 R^3 \Omega^2)$ , is 1000. The droop stop spring stiffness value is chosen because it freezes the flap hinge to less than 0.1 degrees and allows a nondimensional time step of 0.004.

The H-46 aerodynamic blade properties are found in Ref. 22. In this model, the aerodynamic shape of the blade starts at station 67.3 and continues outboard. The blade employs the NACA 0012 airfoil due to the large amount of data available on its unsteady aerodynamics, nonlinear separation and dynamic stall characteristics. The blade is linearly twisted -8.5 degrees from the shaft to the tip (nose down at the tip).

The present research only models the aft rotor system of the H-46. The shaft of the aft rotor system is tilted forward 2.58 degrees with respect to the ship coordinate system. During all rotor engage/disengage sequences, the collective,  $\theta_0$ , is set at 3 degrees and the "auto" cyclic trim setting is selected. The "auto" cyclic trim setting tilts the aft rotor disk 2.5 degrees aft from a plane perpendicular to the shaft axis for a no wind condition. The cyclic control inputs required to obtain this blade response are determined from rigid blade flap dynamics. Assuming negligible inflow and no wind, the longitudinal and lateral cyclic control inputs are 2.5 degrees and 0.0693 degrees, respectively. These control inputs are termed the standard control inputs for the present study and are used to produce all results unless otherwise noted.

#### H-46 Validation

A fan diagram is developed to determine how well the finite element approach models the H-46 flap and torsion rotating natural frequencies. Figure 18 illustrates the first four coupled flap mode frequencies and the first coupled torsion mode frequency. Ref. 21 provides test data for the second through the fourth flap modes which is overlaid in Figure 18 for comparison. The flap-torsion elastic analysis is in satisfactory agreement with the blade data.

The fundamental rotating flap frequency,  $\nu_\beta$ , for a rigid blade flap model can be expressed as

$$\nu_\beta = \frac{1}{2\pi} \sqrt{\frac{K_\beta}{m_0 R^3}} \quad (52)$$

where  $e_f/R$  is the nondimensional flap hinge offset. This model predicts the fundamental flap frequency of 1.013 /Rev for a uniform blade with a hinge offset of 1.7%. The present analysis predicts a fundamental flap frequency of 1.013 /Rev which is exactly the same as the rigid uniform blade prediction.

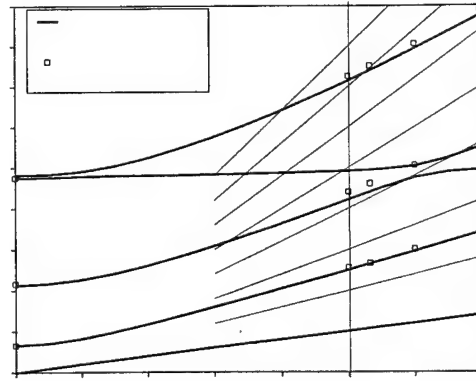


Figure 18: H-46 blade fan diagram (data source: Ref. 21).

The only data available on the torsion frequencies is the fundamental nonrotating frequency with a value of 4.8 /Rev. The blade structural properties with no control system flexibility overpredicts this nonrotating value. Most helicopters require some control system flexibility; therefore, a pitch spring with a nondimensional pitch link stiffness,  $K_\theta/(m_0 R^3 \Omega^2)$ , of  $8.9E-3$  is added to lower the fundamental torsion frequency to 4.8 /Rev.

Proper stiffness and inertia distributions are verified by comparing predicted static tip deflections to experimental data. Ref. 20 provides static tip deflection data of the blade clamped at the two-pin retention. A comparison of these results with the predictions of the finite element model are shown in Figure 19. The static deflection predicted by this

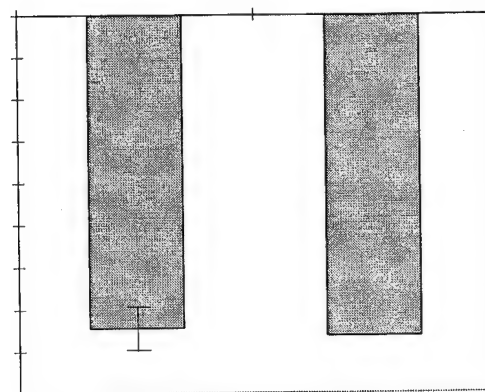


Figure 19: H-46 static tip deflection comparison (data source: Ref. 20).

analysis shows good correlation with the experimental test data.

### Engage/Disengage Analysis

The two baseline aerodynamic environments used in this investigation are a uniform gust and a linearly distributed gust. Both environments are shown in Figure 20 and do not contain ship motion.

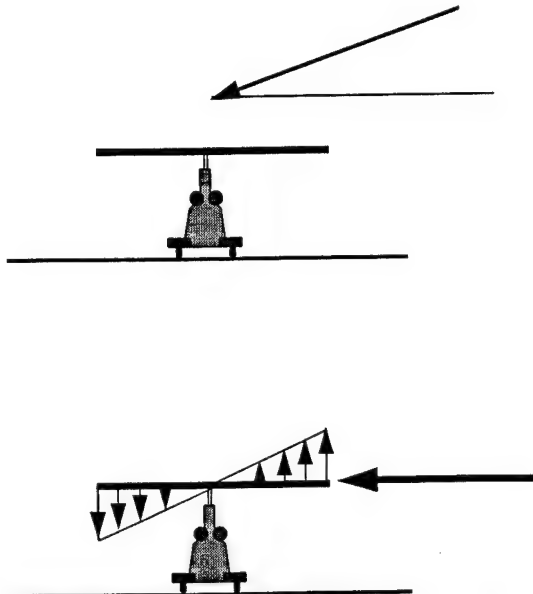


Figure 20: Uniform and linearly distributed gusts.

Note that the angle of the wind above the horizon is  $\alpha_w$ . The uniform gust distribution consists of a 40 knot gust with  $\alpha_w = 15$  degrees. The linearly distributed gust is the same as the deterministic gust model developed in Ref. 8. The wind speed is 40 knots with a 25% upflow through the windward half of the rotor disk and a 25% downflow through the leeward half of the rotor disk. Both gusts approach from the starboard side of the aircraft (WOD direction = 090 degrees).

### ROTOR SPEED PROFILES

The present analysis is capable of computing a transient rotor response for an arbitrary rotor speed time history. The run-up/run-down rotor speed profiles used in this analysis are the same as those in Ref. 9. The run-up and run-down rotor speed time histories were predicted using basic rotor system dynamic and blade aerodynamic laws. During rotor run-up, engine torque was assumed constant and rotor drag torque was assumed to vary as a function of rotor speed squared. The solution took the form of

a hyperbolic tangent function and is shown in Figure 21. The rotor run-down had three phases which included the settling phase, the free spin phase, and braking phase and is shown in Figure 22. The settling phase allowed the numerical solution to reach steady state at the operational rotor speed. The free spin phase modeled the throttle cut-off where only rotor drag torque slows the rotor system. The braking phase modeled brake application as a constant torque and also included the rotor drag torque. This phase ended when the rotor came to a stop.

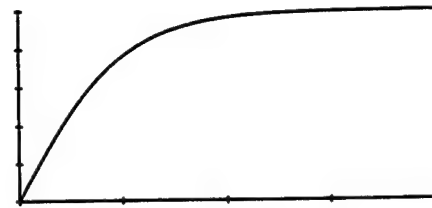


Figure 21: Sea King rotor run-up profile (Source: Ref. 9).

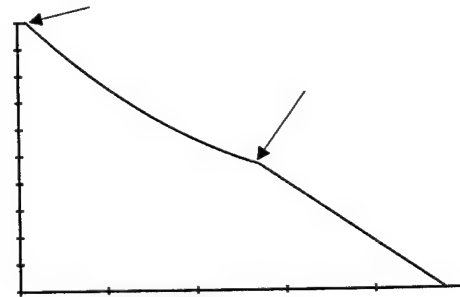


Figure 22: Sea King rotor run-down profile (Source: Ref. 9).

Representative blade responses using the run-up and run-down rotor speed profiles are shown in Figures 23 and 24, respectively. In addition, similar results from Ref. 9 are included in these figures. Note the similar trends between the two predictions. For rotor engagement, the tip deflections decrease as the rotor speed increases. The maximum downward tip deflection occurs within the first two seconds for both models. During rotor disengagement, the blade goes through the three phases described above. As the rotor speed decreases, the blade deflections grow. Note that when the rotor brake is applied, the tip

deflections grow more rapidly and the maximum deflection occurs within the last five seconds. These results show that the blade response trends of this analysis are similar to the ones predicted in Ref. 9.

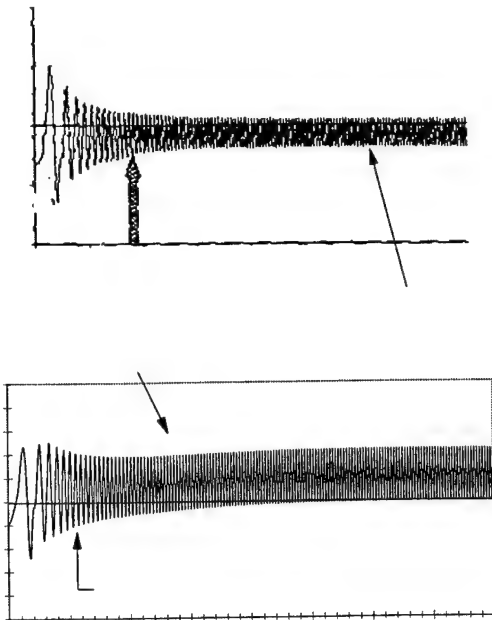


Figure 23: Comparison of transient blade response for rotor engagement.

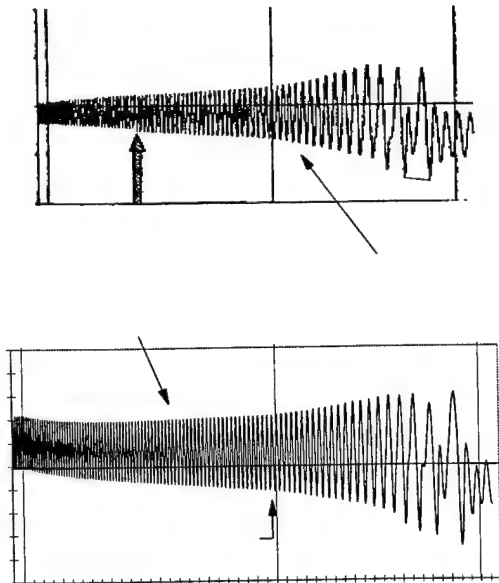


Figure 24: Comparison of transient blade response for rotor disengagement.

## BLADE RESPONSE CHARACTERISTICS

Two types of blade transient response characteristics were observed while conducting this investigation. The tip response of the H-46 blade

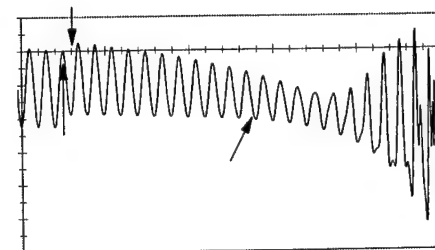
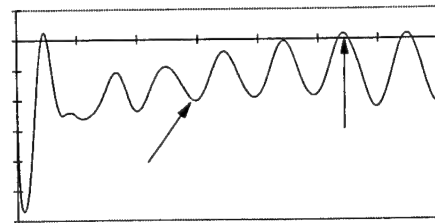


Figure 25: Tip deflection time history for uniformly distributed gust model.

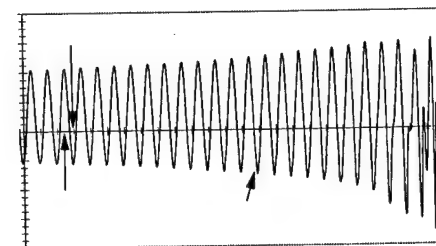
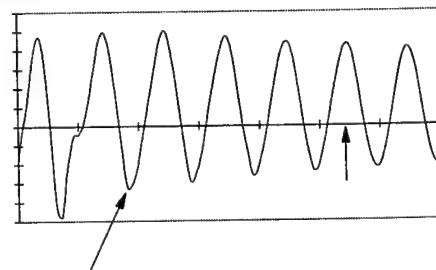


Figure 26: Tip deflection time history for linearly distributed gust model.

subjected to the baseline uniform gust for engage and disengage evolutions is shown in Figure 25. Note for rotor engagement, the aerodynamic forces cause the blade to reach its maximum downward tip deflection in the first revolution. This type of behavior is very prominent for rotor engagement but involves some droop stop interaction for disengagement. The blade transient response to the baseline linear gust distribution for rotor run-up and run-down is shown in Figure 26. The blade response for this wind condition involves substantial blade/droop stop interaction. Note that while the droop stop is initially extended, the blade rises above the hub and then violently strikes the droop stop as the blade tip flies below the hub. The sudden halt of the flap hinge rotation indicates a transfer of system energy from kinetic to potential (strain).

### IMPORTANCE OF TORSION AND UNSTEADY AERODYNAMICS

The purpose of this study is to determine whether higher fidelity models are required for accurate predictions of the tunnel strike phenomenon. The blade transient response for an articulated rotor system is discussed in Ref. 9. This analysis included a torsional component of the flapwise modes in the aerodynamics and predicted aerodynamic loads using quasi-steady theory. The current analysis models a blade undergoing flap and torsion motions and predicts airloads using unsteady aerodynamics. All percent values given in this subsection are based on the tip deflection necessary for fuselage contact (55 inches).

Both flap and flap-torsion structural models are examined. For each structural model, both linear quasi-steady and unsteady with dynamic stall aerodynamic models are utilized for several WOD conditions. The WOD conditions consist of the uniform and linearly distributed gust models at 35 and 45 knots. Figure 27 shows a comparison of the maximum negative tip deflections for a run-up sequence using the uniform gust distribution model. The different aerodynamic and structural models show negligible differences in the 35 knot wind. In the 45 knot wind, large differences (approximately 13%) occur between the aerodynamic models while only small differences are seen between the structural models. These results illustrate the importance of unsteady aerodynamics at wind speeds greater than 35 knots. Overall the differences in structural models is quite small, however, the trends suggest that the flap-torsion model may be more important for winds greater than 45 knots.

The run-up case using the linearly distributed gust model is shown in Figure 28. Similar to the blade response for the uniform gust, unsteady aerodynamics plays a vital role in the prediction of the blade response at high speeds, however, the unsteady aerodynamic model is required for wind speeds lower than 35 knots. Again little accuracy is gained with the flap-torsion model; however, the trends suggest that the flap-torsion model is more important when using the unsteady aerodynamic model at wind speeds greater than 45 knots.

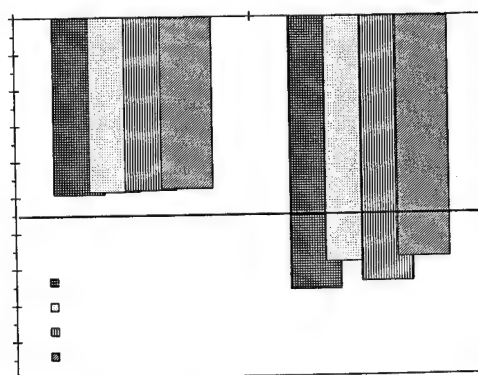


Figure 27 Comparison of structural and aerodynamic models for rotor engagement in a uniformly distributed gust.

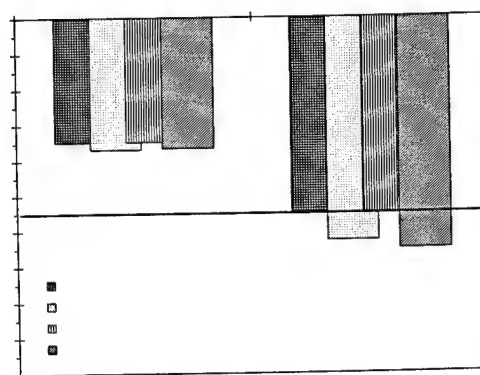


Figure 28: Comparison of structural and aerodynamic models for rotor engagement in a linearly distributed gust.

Overall, note the maximum negative tip deflection trends between the two gust models. In a uniform gust distribution, the maximum downward tip deflections predicted using the unsteady aerodynamic model are smaller than the tip deflections predicted using the quasi-steady model.



Conversely, in a linear gust distribution, the maximum negative tip deflections predicted using the unsteady aerodynamic model are larger than the ones predicted using the quasi-steady model. In addition, unsteady aerodynamics is more important at lower wind speeds for the linearly distributed gust. This study suggests spatially varying gusts may require a higher level of aerodynamic and structural modeling at lower wind speeds than uniform gusts. This analysis recommends a study be conducted that explores the effects of turbulence on blade response during engage/disengage evolutions.

### CONTROL INPUT EFFECTS

The variations of maximum negative tip deflections as a function of collective, longitudinal cyclic and lateral cyclic control inputs are shown in Figures 29, 30, and 31, respectively. The uniformly distributed gust is used to produce these results. During the run-up sequences, the blade response is much more sensitive to collective and lateral cyclic controls as opposed to the longitudinal controls. The change in maximum negative tip deflection for collective and lateral cyclic variations of 4 degrees is approximately 13 inches. The blade response may not be as sensitive to longitudinal controls due to the WOD direction used for this study. Recall that the WOD direction is 90 degrees. This corresponds to an azimuthal location where the longitudinal cyclic control is at its maximum, and additional relative velocity due to the wind speed is lost.

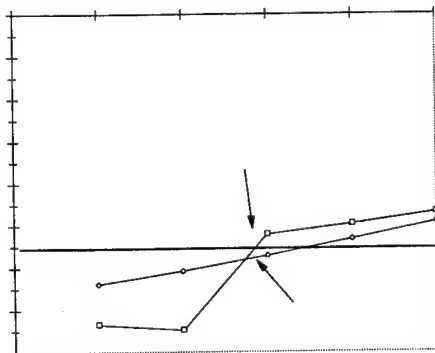


Figure 29: Collective control effects on maximum downward tip deflections

The trends for all three control inputs are linear for the run-up cases which is not the trend for the run-down cases. The tip deflections for lateral cyclic variations are not quite as sensitive for run-down and are slightly shifted up. The trends for the collective

and longitudinal cyclic variations during rotor run-down show a substantial increase in downward tip deflection unlike the run-up cases. Note that as the collective and longitudinal cyclic decrease, the maximum negative tip deflections become much larger. This trend is caused by the droop stop logic for rotor disengagement. For run-down sequences with higher collective and lateral cyclic control settings, the blade is forced to fly higher and the droop stop can extend when centrifugal force allows. At lower control settings, the blade does not fly high

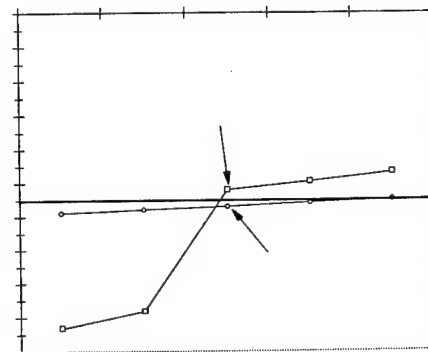


Figure 30: Longitudinal cyclic control effects on maximum downward tip deflections

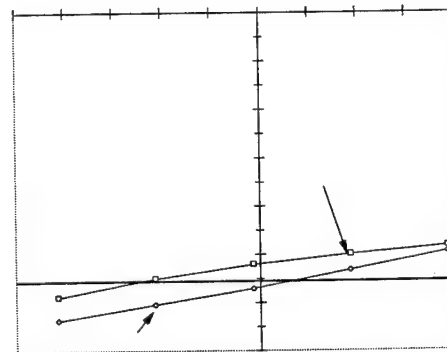


Figure 31: Lateral cyclic control effects on maximum downward tip deflections

enough and physically prevents droop stop activation. Figure 32 shows the effects of droop stop extension on the blade tip deflections. Note how droop stop extension is delayed until much lower rotational speeds. At this point, the blade flaps high enough to allow droop stop extension. These trends suggest that control inputs can reduce maximum negative tip deflections and a study investigating

control effectiveness for other WOD conditions is recommended.

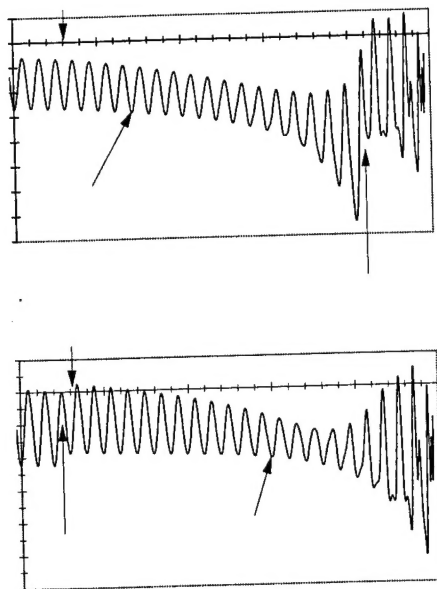


Figure 32: Droop stop behavior effects on maximum downward tip deflection.

### DROOP STOP ANGLE EFFECTS

It is obvious that increasing the droop stop angle increases the static blade/fuselage clearance, however, the effects on the dynamic response of the blade are more unclear. Figure 33 shows the effects of droop stop angle variation on maximum negative tip deflection. Note that for both the run-up and run-down cases, an increase in droop stop angle decreases the maximum tip deflection (increases the blade/fuselage clearance). This observation agrees

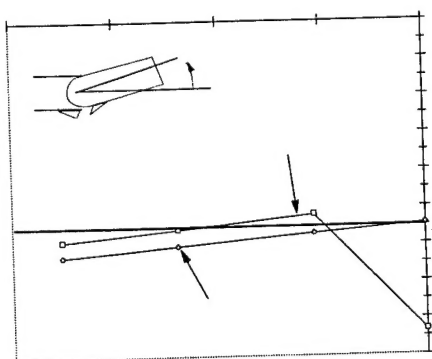


Figure 33: Droop stop angle effects on maximum downward tip deflections

with the static deflection results. The run-down case deviates from the trend for the zero droop stop angle position. Similar to the run-down trends for the collective and longitudinal cyclic controls, the blades flapping motion does not allow droop stop extension. The effectiveness of droop stop rotation on the maximum negative tip deflection is not very large for this WOD condition. Further studies of blade response to droop stop angle variation is recommended for other WOD conditions. But this initial study does not suggest that droop stop angle changes would be an effective means to controlling the tunnel strike phenomenon due to the delay in droop stop extension at higher droop stop angles.

### SHIP MOTION EFFECTS

Preliminary studies of ship motion effects on tip deflections showed the blade response trends to be random for run-down sequences. For these disengage sequence, the ship motion was simulated to start at the same position in its roll motion and only the maximum roll amplitude is varied. Upon further investigation, blade strikes were found to be dependent on ship roll period, maximum roll amplitude and starting position of the ship's roll motion. This study shows the effects of these three ship motion parameters on the tunnel strike phenomenon.

The engage/disengage blade response is simulated for combinations of ship roll period, maximum roll amplitude and starting position in ship roll motion. The roll periods are 3 and 9 seconds and maximum roll amplitudes are 5 and 10 degrees. The ship motion is fixed so that as the blade started during engagements and stopped during disengagements, the ship would be at a specific point in its roll motion. The four specific points in the roll motion included: the ship at the maximum starboard (ship position 2) and port (ship position 4) roll angles, and the ship passing through the zero angle rolling toward the starboard (ship position 1) and port (ship position 3) directions. The blade is subjected to the baseline linear gust distribution. The blade model is the H-46 using the standard engage/disengage control inputs.

The effects of ship motion on the maximum negative tip deflections for rotor engagement are shown in Figure 34. Note for ship positions 1 and 3, the blade response is insensitive to changes in period and maximum amplitude. The blade response for ship positions 2 and 4 to changes in amplitude is large which illustrates that the blade response is very sensitive to the amount of inflow through the rotor disk. For the same ship positions, tip deflections are

insensitive to the roll period. The insensitivity roll period could be due to the rotor speed profile. If acceleration of the rotor system (dependent upon the rotor speed profile) is large compared to the ship motion, the blade does not feel the effects of the ship motion. This becomes clearer upon reviewing the results for rotor disengagement. Lastly note that tip deflections for ship position 4 are, as a whole, larger than those for ship position 2. Previously, the blade was shown to have two blade response characteristics during the low rotor speed regions. All maximum negative tip deflections for ship position 2 are primarily the result of the aerodynamic forces deforming the blade while tip deflections for ship position 4 are primarily the result of blade/droop stop interaction.

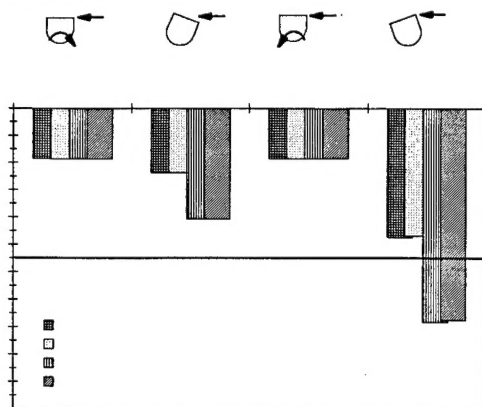


Figure 34: Ship motion effects on maximum downward tip deflections for rotor engagement

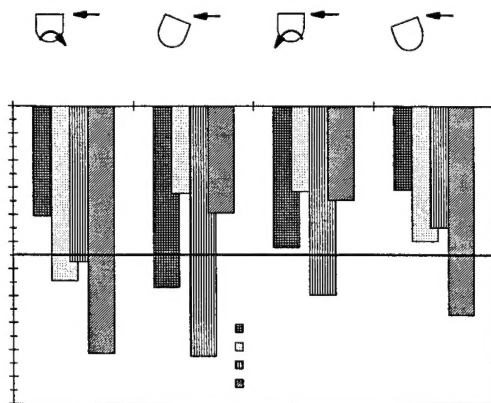


Figure 35: Ship motion effects on maximum downward tip deflections for rotor disengagement

The ship motion effects on the blade response for rotor disengagement are shown in Figure 35. Unlike rotor engagement results, ship motion effects

on the blade response for rotor disengagement are very random. Characteristically slow rotor deceleration in the low rotor speed regions is believed to be the cause of this randomness. The moderate amplitude, large period blade response for ship positions 1 and 4 and moderate amplitude, small period response for ship positions 2 and 3 show very violent blade/droop stop interaction and subsequently much larger negative tip deflections. In contrast, the small amplitude, small period blade response for ship positions 1 and 4 and small amplitude, large period blade response for ship positions 2 and 3 show small negative tip deflections. Overall the tip responses for larger ship roll amplitudes are much higher and more violent than small roll amplitudes.

## CONCLUSIONS

An analysis tool has been developed to predict transient aeroelastic rotor response during rotor engage/disengage sequences. The blade equations of motion are spatially discretized using the finite element method for the elastic flap and torsion degrees of freedom. The discretized blade equations of motion are integrated in time following a rotor speed profile. The analysis employs a semi-empirical unsteady blade element aerodynamic model that is based on an indicial formulation. This research is the first to address the effects of elastic torsion and unsteady aerodynamics on the transient rotor response. In particular, this analysis is used to model H-46 aft rotor system and parameters conducive to the tunnel strike phenomenon are identified.

1) An H-46 rotor system model was developed to investigate parameters conducive to the tunnel strike phenomenon. The blade static tip deflection showed good correlation with experimental data. Blade flap natural frequencies were also verified using experimental data and showed excellent correlation. No torsional natural frequency data was available except for the nonrotating fundamental frequency. The predicted blade natural frequency was too stiff; therefore, control system flexibility was modeled to match the experimental frequency.

2) Blade response characteristics were identified during low rotor speed regions of rotor run-up/run-down. One blade response characteristic suggested that aerodynamic forces were the main contributors to blade deformation while the other suggested that a transfer of system energy from kinetic to potential caused most of the blade deformation.

3) The results illustrated the importance of unsteady aerodynamics at wind speeds greater than 35 knots. The differences in structural models were

quite small, however, the trends suggested that the flap-torsion model may be more important for winds greater than 45 knots.

4) Unsteady aerodynamics was shown to play a vital role in the prediction of the blade response at high speeds, however, the unsteady aerodynamic model was more important for wind speeds lower than 35 knots. Again little accuracy was gained with the flap-torsion model; however, the trends suggested that the flap-torsion model was more important when using the unsteady aerodynamic model at wind speeds greater than 45 knots.

5) Overall larger differences between aerodynamic models and structural models were observed for the linear gust distribution. This study suggested spatially varying gusts may require a higher level of aerodynamic modeling and structural modeling at lower wind speeds.

6) Collective and longitudinal and lateral cyclic control inputs showed a moderate effect on reducing maximum negative tip deflections; however, smaller collective and longitudinal cyclic inputs delay droop stop extension.

7) The droop stop angle had a moderate effect on the tip deflections. This initial study does not suggest that droop stop angle changes would be an effective means to controlling the tunnel strike phenomenon due to the delay in droop stop extension at higher droop stop angles. Ultimately the droop stop could fail to extend which would cause the blade to flap to the ground.

8) During rotor engagement, only the ship start position and ship maximum roll amplitude had a large effect on maximum tip deflections. The largest tip deflections occurred when the ship starts its motion tilted into or away from the wind for both small and moderate maximum roll amplitudes. The ship roll period had no effect on maximum negative tip deflections.

9) During rotor disengagement, tip deflection trends were much more random which was attributed to lower acceleration over the low rotor speed regions. Overall the tip responses for larger ship roll amplitudes were much higher and more violent than small roll amplitudes.

#### ACKNOWLEDGEMENTS

This research was carried out with support from the Naval Air Warfare Center, Aircraft Division located at Patuxent River, MD. In particular, the authors acknowledge our technical monitors, LCDR Bob Drake, Mr. Kurt Long, and Mr. Larry Trick.

#### REFERENCES

1. Val Healey, J., "The Prospects for Simulating the Helicopter/Ship Interface," *Naval Engineers Journal*, March 1987.
2. Carico, G.D., J.W. Groulx, and D.R. Vetter, "H-46 Rotor Engage/Disengage Evaluation Aboard the USS GUADALCANAL(LPH-11)," NAVAIRTESTCEN Report of Test Results FT-49R-74, 18 June 1974.
3. Fowler, J.E., P.W. Martin, and L.L. Trick, "H-46 Dynamic Interface Tests Aboard USS WABASH (AOR-5)," NAVAIRTESTCEN Technical Report RW-94R-84, 4 June 1985.
4. Ball, J.C. and W.R. White, "H-46 Dynamic Interface Tests Aboard USS GUAM (LPH-9)," NAVAIRTESTCEN Technical Report RW-28R-83, 29 March 1984.
5. Hurley, G.E., C.W. Pittman, and L.L. Trick, "HH-46A/CV-64 Rotor Engage/Disengage Test," NAVAIRTESTCEN Report of Test Results RW-55R-84, 30 October 1984.
6. Ruffa, S.A. and E.C. Traasdahl, "CH-46E/LHA-4 Engage/Disengage Dynamic Interface Test," NAVAIRTESTCEN Report of Test Results RW-58R-84, 30 January 1985.
7. Hurst, D.W. and S.J. Newman, "Wind Tunnel Measurements of Ship Induced Turbulence and the Prediction of Helicopter Rotor Blade Response," Eleventh European Rotorcraft Forum Paper No. 99, 10-13 September 1985.
8. Newman, S.J., "A Theoretical Model for Predicting the Blade Sailing Behaviour of a Semi-Rigid Rotor Helicopter," *Vertica*, Vol. 14, No. 4, pp. 531-544, 1990.
9. Newman, S.J., "The Application of a Theoretical Blade Sailing Model to Predict the Behaviour of Articulated Helicopter Rotors," *The Aeronautical Journal of the Royal Aeronautical Society*, June/July 1992.
10. Newman, S.J., "The Problems of Rotor Engagement and Disengagement of a Shipborne Helicopter," *Journal of Naval Sciences*, Vol. 20, No. 1, 1994.

11. Ferrier, B. and J. Semenza, "NATC Manned Flight Simulator VTOL Ship Motion Simulation and Application," Presented at the 46th Annual National Forum of the American Helicopter Society, Washington, D.C., May 1990.
12. Geyer, W. P., "Aeroelastic Analysis of Transient Blade Dynamics during Shipboard Engage/Disengage Operations," Pennsylvania State University Thesis, August 1995.
13. Smith, E.C., "Aeroelastic Response and Aeromechanical Stability of Helicopters with Elastically Coupled Composite Rotor Blades," University of Maryland Thesis, UM-AERO 92-15, 31 July 1992.
14. Bir, G. and Inderjit Chopra, "University of Maryland Advanced Rotorcraft Code (UMARC) Theory Manual," University of Maryland, UM-AERO 92-02, College Park, MD, 7 August 1992.
15. Johnson, W., *Helicopter Theory*, Dover Publications, Inc., New York, 1994.
16. Beddoes, T.S. and J.G. Leishman, "A Generalised Model for Airfoil Unsteady Aerodynamic Behavior and Dynamic Stall using the Indicial Method," Presented at the 42nd. Annual Forum of the American Helicopter
17. Beddoes, T.S. and J.G. Leishman, "A Semi-Empirical Model for Dynamic Stall," *Journal of the American Helicopter Society*, July 1989.
18. Leishman, J.G., *Unsteady Aerodynamic Theory Manual for the Technology Complex (TC) Airloads and Induced Velocity (ALIV) CPCI of the Second Generation Comprehensive Helicopter Analysis (2GCHAS)*, University of Maryland, College Park, July 1990.
19. Smith, P. and W. Trainer, "H-46 Modified Droop Stop Investigation," NAVAIRTESTCEN Quick Response Report RW-75R-86, 26 September 1986.
20. Thompson, G.H., "CH-46 Tunnel Clearance Metal vs Fiberglass Blades," Boeing Vertol Company Interoffice Memorandum, 2 June 1982
21. "Theoretical Physical Properties of the A02R1702 Composite Rotor Blade," Boeing Vertol Company Report #A02-SS-027-1, Philadelphia, PA, 28 March 1977.
22. "Helicopter Flying Qualities Characteristics - CH-46E Volume 1," Boeing Vertol Company Report # NADC-81118-60, Philadelphia, PA, undated.